CRYSTAL GROWTH & DESIGN

pubs.acs.org/crystal

Article

Tribenzyl(methyl)ammonium: A Versatile Counterion for the Crystallization of Nanojars with Incarcerated Selenite and Phosphite Ions and Tethered Pyrazole Ligands

Wisam A. Al Isawi, Matthias Zeller, and Gellert Mezei*

Cite This: *Cryst. Growth Des.* 2022, 22, 1398−1411

Read Online

ACCESS | Metrics & More | Article Recommendations | Supporting Information

ABSTRACT: One hundred and thirty-five years after its initial discovery, the crystal structure of the tribenzyl(methyl)ammonium ($TBMA^+$) cation is reported for the first time (as the nitrate salt). It is shown that $TBMA^+$ is an excellent counterion for the crystallization of large supramolecular assemblies. Thus, single crystals of previously uncrystallizable nanojars with incarcerated selenite and phosphite ions, as well as tethered pyrazole ligands, have been successfully grown by solvent vapor diffusion into solutions with added $(TBMA)NO_3$. X-ray diffraction studies reveal a variety of possible noncovalent interactions between pairs of $TBMA^+$ cations. Indeed, the structurally adaptable $TBMA^+$ dimer can take on different shapes and sizes to maximize supramolecular interactions with neighboring molecules and to fill up voids in the crystal lattice. The new nanojar crystal structures $(TBMA)(Bu_4N)[SeO_3{\subset}\{Cu(OH)(pz)\}_{28}]$ and $(TBMA)_2[HPO_3{\subset}\{Cu(OH)(pz)\}_{29}]$ (pz = pyrazolate) provide unprecedented examples of noncovalently bound selenite and phosphite ions in supramolecular complexes. The use of $TBMA^+$ counterions has also allowed for the crystallization of a nanojar based on tethered pyrazole ligands, $(TBMA)_2[SO_4{\subset}\{Cu_{28}(OH)_{28}(pzCH_2CH_2pz)_{14}\}]$. The synthesis and mass spectrometric studies of the new nanojars are presented along with crystallographic studies detailing the nanojar structure, anion binding, and nanojar−counterion/counterion−counterion supramolecular interactions in the crystal lattice. Finally, the binding of SeO_3^{2-} and SO_4^{2-} ions by the same Cu_{28} nanojar and the binding of HPO_3^{2-}, CO_3^{2-}, and SO_4^{2-} ions by the same Cu_{29} nanojar are contrasted, and the δ/λ chelate-ring isomerism in the tethered-ligand nanojar is discussed.

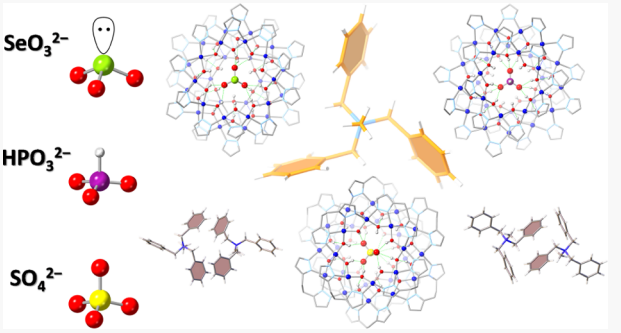

INTRODUCTION

Small inorganic anions are ubiquitous in Nature, and many of them, including halides, bicarbonate, phosphate, and sulfate, are essential for living organisms. Other anions such as arsenate and chromate are highly toxic and carcinogenic.[1] Although selenium is an essential trace element for both humans and animals, selenium oxyanions (selenate and selenite) are highly toxic.[2] Selenium pollution can originate from both natural and anthropogenic sources, including mining, petrochemical, agricultural, and industrial manufacturing operations.[3] The nontoxic phosphite anion, HPO_3^{2-}, is also encountered in the environment, and it plays an important role in the biogeochemistry of phosphorus[4−6] and in agriculture.[7,8] The accumulation in water bodies of otherwise harmless anions, such as phosphate from fertilizers[9] and chloride from road salt,[10] is detrimental for the environment. Therefore, the study of anion binding and the development of anion receptors for the recognition and selective extraction of anions from aqueous media is an important current field of study. While living organisms employ specialized proteins for their recognition and transport, the selective binding of small inorganic anions by artificial receptors is a challenging task. In anion binding proteins, the anion is located in a binding pocket, surrounded by a multitude of amino acid residues that form charge-assisted hydrogen bonds with the anion.[11] Synthetic anion binding systems are also based on noncovalent interactions.[12] In many cases, however, the lack of a rigid backbone, such as that found in proteins, is detrimental for both binding strength and selectivity. Several books[13−16] and recent review articles[17−37] have summarized the current state of the art of supramolecular anion recognition and transport.[38,39]

A distinct class of anion binding agents, termed nanojars, consists of a series of supramolecular coordination complexes of the formula $[anion^{2-}{\subset}\{Cu(\mu\text{-}OH)(\mu\text{-}pz)\}_n]^{2-}$ (Cu_n, n = 26−36; pz = pyrazolate anion or a derivative).[40,41] Nanojars are based on three or four neutral $\{cis\text{-}Cu(\mu\text{-}OH)(\mu\text{-}pz)\}_x$ metallamacrocycles (x = 6−14, except 11) bound to each other by an

Received: November 18, 2021
Revised: January 5, 2022
Published: January 17, 2022

https://doi.org/10.1021/acs.cgd.1c01361
Cryst. Growth Des. 2022, 22, 1398−1411

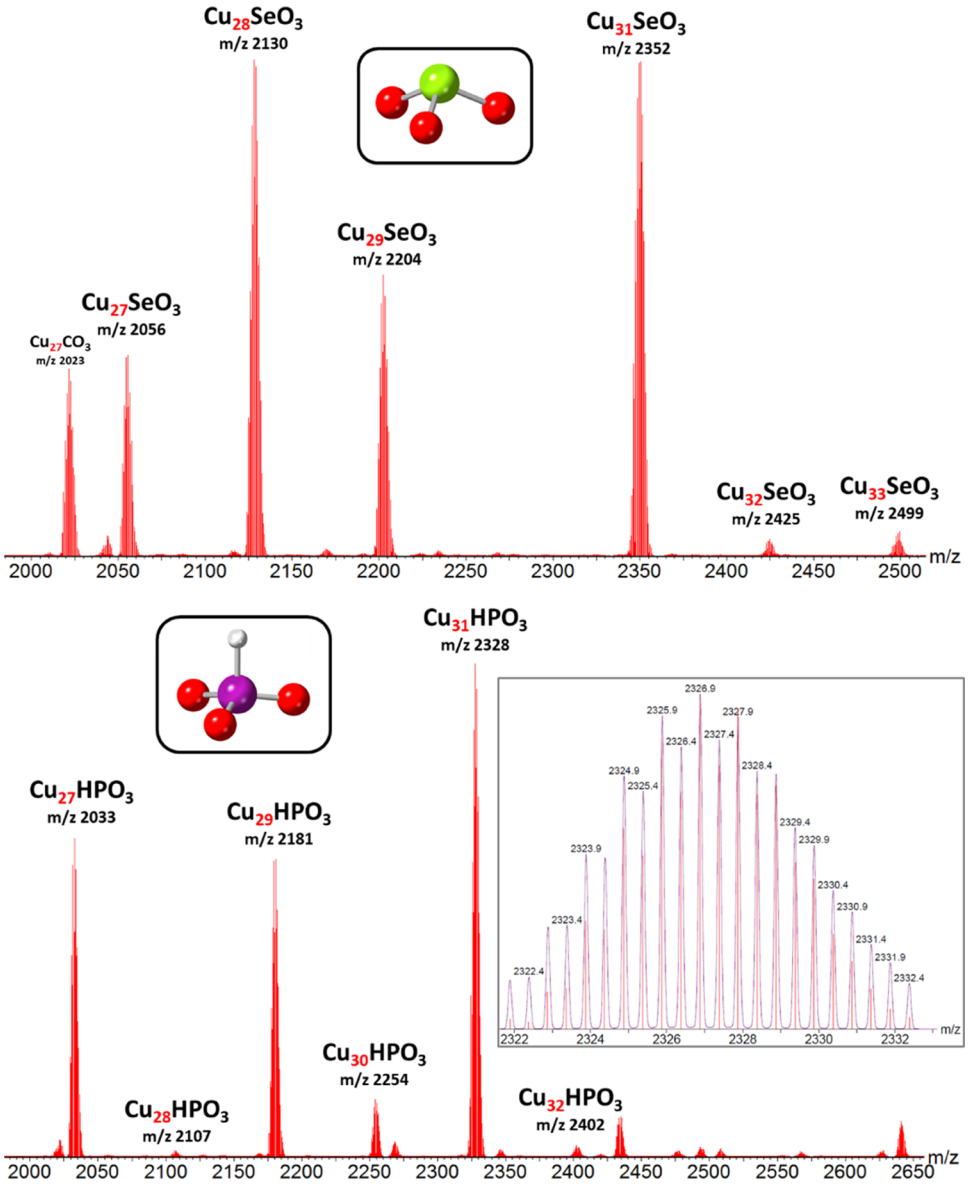

Figure 1. ESI-MS spectra in CH_3CN of the selenite-incarcerating nanojars $[SeO_3\subset\{Cu(OH)(pz)\}_n]^{2-}$ (n = 27−29, 31−33) and phosphite-incarcerating nanojars $[HPO_3\subset\{Cu(OH)(pz)\}_n]^{2-}$ (n = 27−32). The isotopic distribution of $Cu_{31}HPO_3$ (continuum, predicted; centroid, observed) is shown in the inset, and that of other major peaks is given in Figure S1.

intricate network of H-bonding and axial Cu···O interactions and possess an inner anion binding pocket similar to those in anion-binding proteins. In nanojars, this pocket is lined by a multitude of H-bond donors (OH groups), which wrap around the incarcerated anion and completely isolate it from the surrounding medium. Some of the advantages of nanojars as anion-binding agents are the ease of preparation by self-assembly from simple, readily available building blocks,[42] tunable solubility in a wide variety of solvents,[43] extremely strong binding of the incarcerated anion,[44] thermal robustness,[45] and stability to extreme alkalinities.[42] Most importantly, nanojars can be made selective for different anions by tethering pairs of pyrazole ligands together. Thus, nanojars can selectively bind either carbonate or sulfate from an equimolar mixture of the two anions by using either an ethylene or a propylene tether between pairs of pyrazole moieties.[46,47]

With incarcerated CO_3^{2-}, SO_4^{2-}, HPO_4^{2-}, and $HAsO_4^{2-}$ ions, single crystals suitable for X-ray diffraction were readily obtained by vapor diffusion of hexane into toluene solutions of the $(Bu_4N)_2[anion\subset\{Cu(OH)(pz)\}_n]$ nanojars.[41,48,49] With other anions, such as SeO_3^{2-} and HPO_3^{2-} described here, no suitable crystals could be obtained using the same solvent system. Subsequent efforts utilizing a wide range of different solvent combinations, as well as other tetraalkylammonium (Me_4N^+, Et_4N^+) and tetrabutylphosphonium (Bu_4P^+) counterions, also yielded no suitable crystals. Similar work aimed at crystallizing nanojars with tethered pyrazole ligands, $(Bu_4N)_2[anion\subset\{Cu_n(OH)_n(pzCH_2CH_2pz)_{n/2}\}]$ (anion = CO_3^{2-}, SO_4^{2-}; $pzCH_2CH_2pz$ = 1,2-bis(pyrazol-3(5)-yl)ethane dianion), has also been unsuccessful. We anticipated that a counterion possessing aromatic groups might aid in the formation of a more robust crystal lattice, as the pyrazolate moieties of the nanojar could form favorable aromatic interactions with the counterions. Despite the fact that they contain multiple phenyl moieties, both tetraphenylphosphonium (Ph_4P^+) and bis(triphenylphosphoranylidene)ammonium

https://doi.org/10.1021/acs.cgd.1c01361
Cryst. Growth Des. 2022, 22, 1398−1411

(PPN^+) failed to provide nanojar single crystals. This might be attributed to the fact that the phenyl moieties of Ph_4P^+ and PPN^+ are rigidly anchored onto the central P atom and their only flexibility arises from rotation around the P−C bond. To introduce more flexibility into the aromatic counterion, we then considered tribenzyl(methyl)ammonium. In $TBMA^+$, the aromatic groups have additional flexibility due to free rotation of the benzyl moieties around the N−C bond, in addition to free rotation of the phenyl groups around the C−C bonds to the CH_2 units. Although $TBMA^+$ was synthesized 135 years ago,[50] there is no report of its use as a counterion and no structure containing this cation is available in the Cambridge Structural Database. As had been hoped, $TBMA^+$ does lead to favorable aromatic interactions with nanojars and allowed for the successful growth of single crystals of nanojars that were previously obtainable only as amorphous or microcrystalline solids. Herein we present the synthesis and mass-spectrometric characterization of novel selenite- and phosphite-incarcerating nanojars, along with the detailed crystal and molecular structures of $(TBMA)NO_3$, $(TBMA)(Bu_4N)[SeO_3\subset\{Cu(OH)(pz)\}_{6+12+10}]$ (**1**), $(TBMA)_2[HPO_3\subset\{Cu(OH)(pz)\}_{8+13+8}]$ (**2**), and $(TBMA)_2[SO_4\subset\{Cu(OH)(pzCH_2CH_2pz)_{0.5}\}_{8+12+8}]$ (**3**).

RESULTS AND DISCUSSION

Synthesis and Mass Spectrometric Studies. Tribenzyl(methyl)ammonium iodide was synthesized by the reaction of tribenzylamine with excess methyl iodide at room temperature. To prevent interference from iodine (such as partial iodination of the pyrazole 4-position) formed by the possible oxidation of iodide during crystallization of nanojars, the iodide salt of the cation was converted to the nitrate salt by metathesis with $AgNO_3$. Nanojars are known to be stable even in the presence of a large excess of nitrate ions.[41]

Nanojars with incarcerated selenite or phosphite ions were obtained by the room-temperature reaction of copper(II) nitrate, pyrazole, sodium selenite or phosphite, NaOH, and Bu_4NOH in a 1:1:1:1.93:0.07 molar ratio in tetrahydrofuran. The general mechanism of formation of nanojars by self-assembly, leading to different nanojar sizes, was described earlier.[42] In the case of the selenite-incarcerating nanojars, ESI-MS(−) indicates the presence of $[SeO_3\subset\{Cu(OH)(pz)\}_n]^{2-}$ species at m/z 2056 (n = 27), m/z 2130 (n = 28), m/z 2204 (n = 29), m/z 2352 (n = 31), m/z 2425 (n = 32), and m/z 2499 (n = 33), with $Cu_{28}SeO_3$ and $Cu_{31}SeO_3$ being the most abundant species (Figure 1). For the phosphite-incarcerating nanojars, ESI-MS(−) shows $[HPO_3\subset\{Cu(OH)(pz)\}_n]^{2-}$ species at m/z 2033 (n = 27), m/z 2107 (n = 28), m/z 2181 (n = 29), m/z 2254 (n = 30), m/z 2328 (n = 31), and m/z 2402 (n = 32), with $Cu_{31}HPO_3$ being the most abundant species (Figure 1).

Crystallographic Studies. In the crystal lattice of $(TBMA)NO_3$, the $TBMA^+$ cation is located on a general position and displays a pseudo-3-fold symmetry (Figure 2). One of the benzyl groups is disordered over two positions. The nitrate anion, as well as an ethanol and an H_2O solvent molecule, is heavily disordered. Details of the disorder are described in the Experimental Section, and a thermal ellipsoid plot showing the disorder (Figure S2) along with a packing diagram (Figure S6) are provided in the Supporting Information.

*$(TBMA)(Bu_4N)[SeO_3\subset\{Cu(OH)(pz)\}_{6+12+10}]$ (**1**).* In the crystal lattice of **1**·solvent (solvent = 1,2-dichlorobenzene, benzonitrile, hexane) the nanojar unit, composed of three neutral $[cis\text{-}Cu^{II}(\mu\text{-}OH)(\mu\text{-}pz)]_n$ rings (n = 6 + 12 + 10), is located on a general position and displays pseudomirror symmetry relative to two orthogonal mirror planes (one of them containing a Se−O bond) perpendicular to the metallamacrocycles (Figure 3). The central SeO_3^{2-} anion is disordered over two positions by an approximately 180° rotation around the axis containing its lone pair of electrons. A thermal ellipsoid plot showing the disorder is provided in the Figure S3 in the Supporting Information, and bonding data are summarized in Tables S1, S2, and S5.

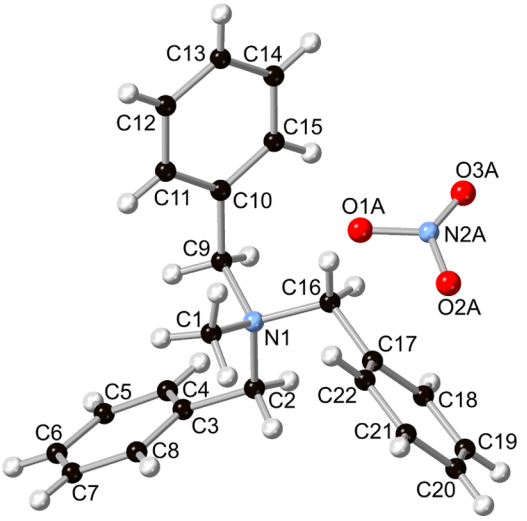

Figure 2. Ball and stick representation of the crystal structure of $(TBMA)NO_3$. The disordered ethanol and water solvent molecules are omitted for clarity, and only one component is shown for the disordered benzyl and nitrate moieties.

Only one of the two original Bu_4N^+ counterions was replaced by $TBMA^+$ during the crystallization process to produce single crystals of **1** suitable for X-ray diffraction. As shown in Figure 4, the $TBMA^+$ counterions are located next to the larger Cu_{10} side ring of the nanojar and are disordered (1:1) across an inversion center over two half-occupied positions. The other, smaller Cu_6 side ring of the nanojar accommodates a butyl arm of the Bu_4N^+ counterion. The bowl-shaped Cu_{10} rings of adjacent nanojars define a cavity occupied by two disordered $TBMA^+$ counterions (Figure 5). A closer inspection of the structure of the two distinct $TBMA^+$ moieties reveals that its phenyl groups adopt several different orientations relative to the central N atom, facilitated by the benzyl CH_2 groups (Figure 6). The packing diagram of **1** shows that the nanojar units are packed in a hexagonal pattern along the *ac* plane and are stacked in columns along the *b* axis (Figure 5).

The structure of the $Cu_{28}SeO_3$ nanojar host is almost superimposable with that of $Cu_{28}SO_4$.[41] However, the SeO_3^{2-} ion is bound very differently from the SO_4^{2-} ion. As seen in Figure 7, the SeO_3^{2-} and SO_4^{2-} ions have opposite orientations in the cavity of the nanojar host. Thus, each O atom of the SeO_3^{2-} ion forms one H bond with the Cu_6 ring of the nanojar (O···O range, 2.743(18)−2.803(15) Å; average, 2.77(1) Å) and two H bonds with the Cu_{10} ring (O···O range, 2.684(18)−2.948(9) Å; average, 2.86(1) Å), with the lone pair of electrons of the Se atom oriented outward through the center of the Cu_{10} ring. In the case of the SO_4^{2-} ion, three O atoms form two H bonds each with the Cu_{10} ring of the nanojar (O···O range, 2.730(14)−2.962(12) Å; average, 2.85(1) Å), whereas the fourth O atom points inward toward the Cu_6 ring to form six H bonds with its OH groups (O···O range, 2.946(5)−3.080(7) Å; average, 3.009(5) Å) (Figure 8). The different binding patterns of the two anions within the same nanojar is not surprising, as

https://doi.org/10.1021/acs.cgd.1c01361
Cryst. Growth Des. 2022, 22, 1398−1411

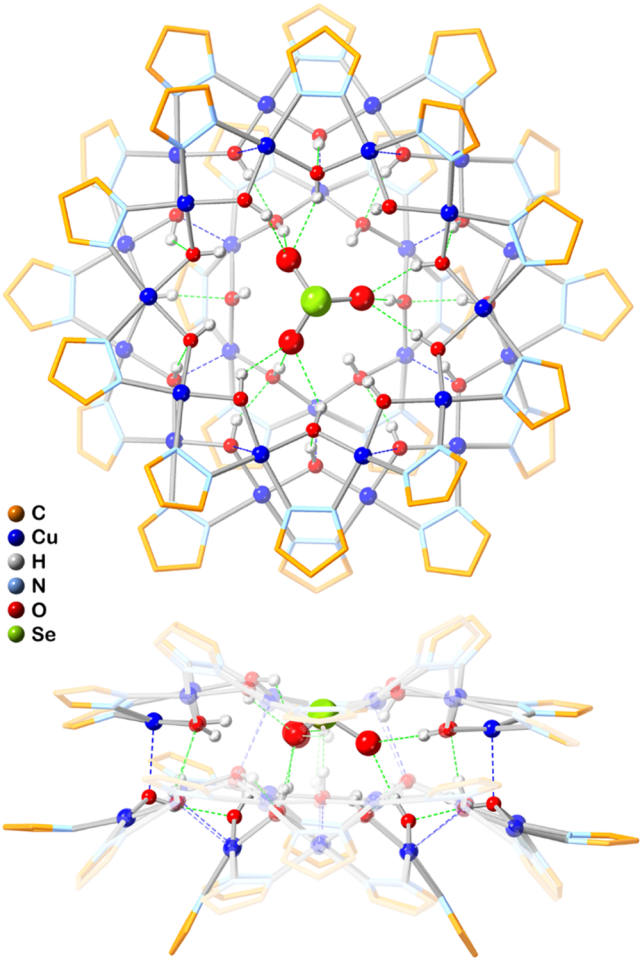

Figure 3. Ball and stick representations of the crystal structure of **1** (top and side views). Green and blue dotted lines indicate O−H···O hydrogen bonds and axial Cu···O interactions, respectively. Counterions, lattice solvent molecules, and C−H bond H atoms are omitted for clarity, and only one component is shown for disordered selenite and pyrazolate moieties.

the structures of the anions are quite different. The difference in size between the anions is based on two opposing factors: the average Se−O bond length of 1.691(10) Å in SeO_3^{2-} is larger than the average S−O bond length of 1.473(7) Å in SO_4^{2-},[51] whereas the stereoactive lone pair of electrons on the Se atom decreases the average O−E−O angle from 109.5° in SO_4^{2-} to 102.4° in SeO_3^{2-}.[52] Overall, the SeO_3^{2-} ion is larger than the SO_4^{2-} ion, with average O···O distances of 2.635 Å in SeO_3^{2-} and 2.399 Å in SO_4^{2-}.[52] As illustrated in Table 1, the increase in anion size is correlated with a shortening of the average H-bonding distance between the OH groups of the $Cu_{6+12+10}$ nanojar and the incarcerated anion (from 2.93(1) to 2.82(1) Å). Anion-binding proteins can also bind different oxyanions in the same protonation state. Although no crystal structure of a selenite transport protein is yet available, it has been shown that in bacteria the same protein can transport sulfate, selenate, and selenite.[53] Nevertheless, sulfate is bound 5 times more strongly than selenate and 37 times more strongly than selenite.

(TBMA)$_2$[HPO$_3$⊂{Cu(OH)(pz)}$_{8+13+8}$] (**2**). In the crystal lattice of **2**·solvent (solvent = nitrobenzene, pentane) the nanojar unit, composed of three neutral $[cis\text{-}Cu^{II}(\mu\text{-}OH)(\mu\text{-}pz)]_n$ rings (n = 8 + 13 + 8), is located on a 2-fold rotation axis running through the center of the nanojar and bisecting the Cu_{13} ring (Figure 9).

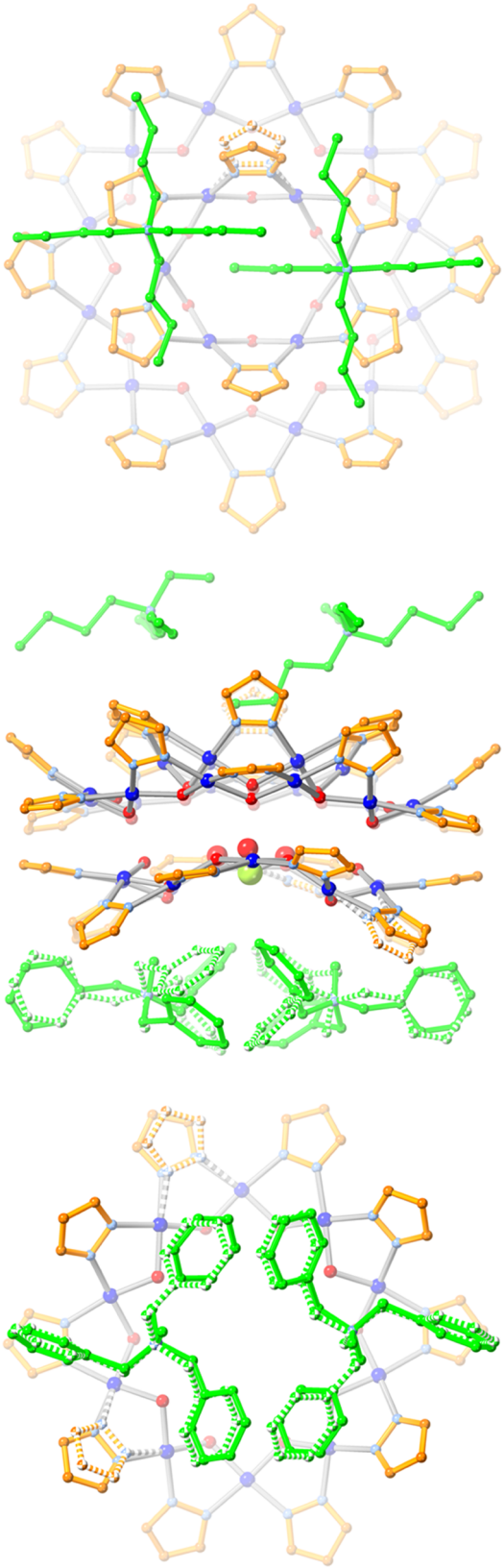

Figure 4. Illustration of the positions of the Bu_4N^+ and disordered $TBMA^+$ counterions in the crystal structure of **1**.

Thus, one complete Cu_8 ring and half of the Cu_{13} ring are found in the asymmetric unit. The HPO_3^{2-} anion is also 2-fold disordered around the C_2 rotation axis; additionally, the three O atoms of the HPO_3^{2-} units are each disordered over three

https://doi.org/10.1021/acs.cgd.1c01361
Cryst. Growth Des. 2022, 22, 1398−1411

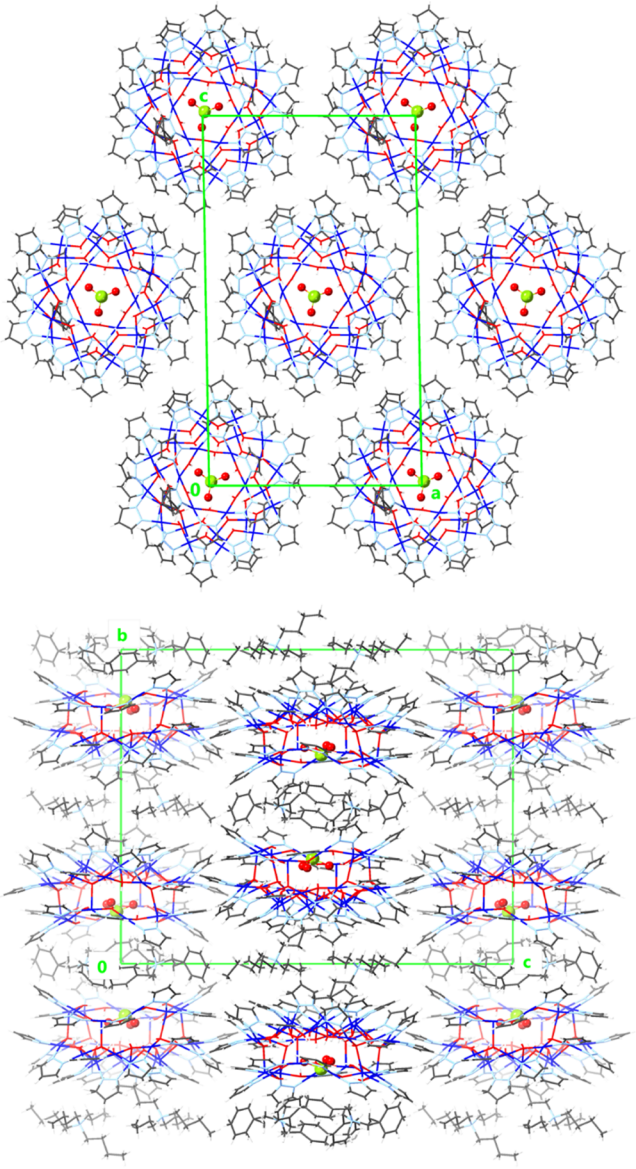

Figure 5. Packing diagrams of **1** showing views down the *b* (one layer only, without counterions) and *a* axes. Lattice solvent molecules are omitted for clarity, and only one component is shown for disordered selenite and pyrazolate moieties.

general positions. A thermal ellipsoid plot showing the disorder is provided in Figure S4 in the Supporting Information, and bonding data are summarized in Tables S1, S3, and S6.

As opposed to **1**, both original Bu_4N^+ counterions were replaced by $TBMA^+$ during the crystallization process of **2**. Pairs of $TBMA^+$ counterions, related by an inversion center as in **1**, are located in cavities formed by the bowl-shaped Cu_8 rings of adjacent nanojars (Figure 10). In contrast to **1**, in which layers of nanojars and counterions alternate, the nanojar layers in **2** are next to each other and nanojar units are not stacked but rather are offset. The packing diagram of **2** shows that the nanojar units are packed in a slightly offset square pattern, as opposed to the hexagonal packing in **1** (Figure S7).

In addition to $Cu_{29}HPO_3$, the Cu_{8+13+8} ring combination has also been observed previously with carbonate[48] and sulfate ions.[45] Although they are rather similar, the nanojar host structures in these three assemblies are not quite super-

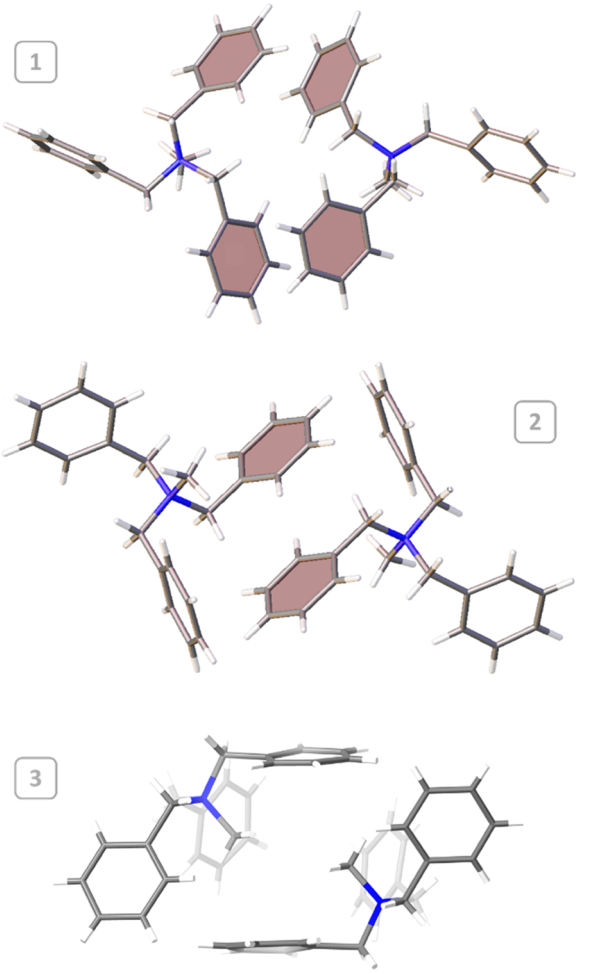

Figure 6. Illustration of the versatility of interactions between pairs of $TBMA^+$ cations in **1**–**3**. Aromatic π–π stacking interactions are highlighted by shaded phenyl rings.

imposable as in the case of $Cu_{28}SeO_3/Cu_{28}SO_4$ (Figure 11). The position of the CO_3^{2-}, HPO_3^{2-}, and SO_4^{2-} ions inside the Cu_{8+13+8} nanojar cavity is shown in Figure 12. Each O atom of the HPO_3^{2-} ion forms three H bonds: two with a Cu_8 ring on one side of the nanojar and one with the Cu_8 ring on the opposite side (O···O range, 2.66(2)–2.93(2) Å; average, 2.77(2) Å). In $Cu_{29}CO_3$ and $Cu_{29}SO_4$, which are also bisected by a C_2 rotation axis, the corresponding values are O···O range 2.794(7)–3.018(6) Å, average 2.855(7) Å and O···O range 2.67(1)–3.014(5) Å, average 2.82(1) Å, respectively. While the stereoactive lone pair on Se decreased the average O–E–O angle from 109.5° in SO_4^{2-} to 102.4° in SeO_3^{2-}, the hydrogen atom in HPO_3^{2-} increases the corresponding average angle to 112.4°. This larger angle, together with a longer average P–O distance of 1.516 Å, makes the HPO_3^{2-} ion larger than both the CO_3^{2-} and SO_4^{2-} ions. As seen above with the $Cu_{6+12+10}$ nanojar, the increase in anion size is again correlated with a shortening of the average H-bonding distance between the OH groups of the Cu_{8+13+8} nanojar and the incarcerated anion (from 2.855(7) to 2.77(2) Å) (Table 1).

Phosphite binding by bacterial proteins has been studied,[54,55] and it has been shown that the binding is pH dependent. No binding was observed at neutral pH; instead, the hydrogenphosphite (HPO_3H^-) ion is bound at pH 5. In addition to a number of H bonds between the HPO_3H^- ion and various

https://doi.org/10.1021/acs.cgd.1c01361
Cryst. Growth Des. 2022, 22, 1398–1411

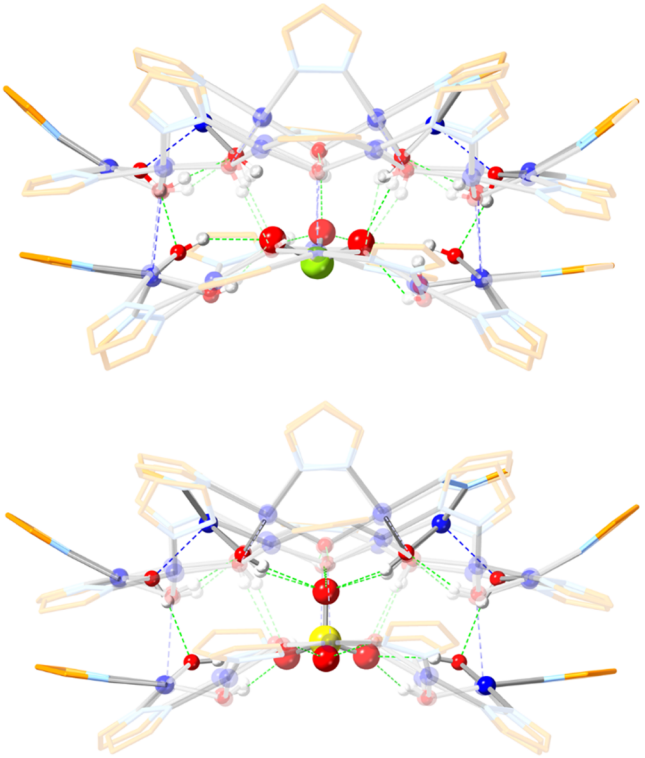

Figure 7. Structural comparison of the nanojars in $(TBMA)(Bu_4N)[SeO_3\subset\{Cu(OH)(pz)\}_{6+12+10}]$ (**1**) and $(Bu_4N)_2[SO_4\subset\{Cu(OH)(pz)\}_{6+12+10}]$.[41] Only one component is shown for disordered selenite, sulfate, and pyrazolate moieties. Green and blue dotted lines indicate O−H···O hydrogen bonds and axial Cu···O interactions, respectively.

amino acid residues, there is also a P−H···π interaction with a tryptophan residue present in the anion-binding pocket of the protein. In the Cu_{8+13+8} nanojar, the hydrogen atom of the incarcerated HPO_3^{2-} ion points outward through the center of the Cu_8 ring.

$(TBMA)_2[SO_4\subset\{Cu_{28}(OH)_{28}(pzCH_2CH_2pz)_{14}\}]$ (**3**). In the crystal lattice of **3**·solvent (solvent = nitrobenzene, pentane) utilizing the tethered $pzCH_2CH_2pz$ ligand, the nanojar unit, composed of three neutral $[cis\text{-}Cu^{II}(\mu\text{-}OH)(\mu\text{-}pz)]_n$ rings (n = 8 + 12 + 8), is again located on a 2-fold rotation axis running through the center of the nanojar and bisecting the Cu_{12} ring (Figure 13). Similarly to **2**, one complete Cu_8 ring and half of the Cu_{12} ring are found in the asymmetric unit, and the SO_4^{2-} anion is 2-fold disordered around the C_2 rotation axis. The two O atoms of the SO_4^{2-} ion located above and below the Cu_{13} ring mean plane each form three H-bonds with the nearby Cu_8 ring, whereas the two O atoms located along the Cu_{13} ring mean plane each form two H bonds with one Cu_8 ring and one H bond with the other Cu_8 ring (O···O range, 2.74(2)−3.00(2) Å; average, 2.89(2) Å). A thermal ellipsoid plot showing the disorder is provided in Figure S5 in the Supporting Information, and bonding data are summarized in Tables S1, S4, and S7.

As in **2**, both original Bu_4N^+ counterions were replaced by $TBMA^+$ during the crystallization process of **3**. The whole $TBMA^+$ molecule is disordered over two positions (Figure 14). As in **1** and **2**, pairs of neighboring $TBMA^+$ counterions are related by an inversion center and are located in cavities formed by the bowl-shaped Cu_8 rings of adjacent nanojars. The packing diagram of **3** shows that the nanojar units are packed in a square pattern along the *bc* plane and are offset along the *a* axis (Figure S8). While in **1** nanojars from adjacent layers are stacked, in **3** nanojars in every other layer are stacked.

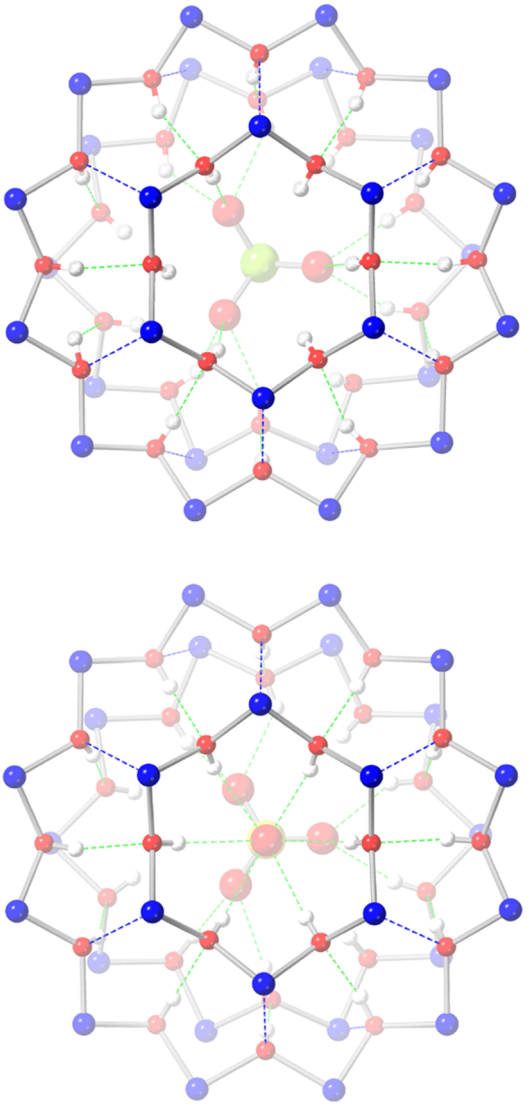

Figure 8. Structural comparison of the anion-binding pockets of the Cu_{28} selenite (**1**) and sulfate nanojars showing their $Cu_{6+12+10}SeO_3$ and $Cu_{6+12+10}SO_4$ cores, respectively (only one component is shown for the disordered selenite and sulfate moieties). Green and blue dotted lines indicate O−H···O hydrogen bonds and axial Cu···O interactions, respectively.

Due to a ring twist of the seven-membered chelate rings formed by the tethered ligand $pzCH_2CH_2pz$, δ/λ isomerism is observed in **3**. While both δ and λ conformations are possible for all of the CH_2CH_2 groups, only a $\delta\delta\delta\delta$ conformation is observed for the Cu_8 ring and a $\lambda\delta\delta\lambda\delta\delta$ conformation for the Cu_{12} ring (Figure 15). In the latter, the two λ ligand conformations are located on the C_2 axis of rotation.

As was observed in the three nanojar structures described here, pairs of $TBMA^+$ ions adopt different shapes and sizes (longest distance between H atoms at the periphery of the dimer: 19.2523(5) Å in **1**, 19.489(7) Å in **2**, and 15.0557(5) Å in **3**) to fill up cavities in the crystal lattice created by the bowl-shaped side rings of adjacent nanojars. In **1**, adjacent $TBMA^+$ moieties form $\pi-\pi$ stacking interactions between two pairs of phenyl groups with centroid···centroid distances of 3.860(13) and 3.920(11) Å and plane···plane separations of 3.19(3)/

https://doi.org/10.1021/acs.cgd.1c01361
Cryst. Growth Des. 2022, 22, 1398−1411

Table 1. Structural Parameters of the CO_3^{2-}, SO_4^{2-}, HPO_3^{2-}, and SeO_3^{2-} Ions along with H-Bonding Data

	av E−O (Å)	av O−E−O (deg)	av O···O within anion (Å)	donor/acceptor O···O range for H bonds to anion (Å)	av O···O distance for H bonds to anion (Å)
CO_3^{2-}	1.284	120.0	2.214	2.794(7)−3.018(6) (Cu_{8+13+8})	2.855(7)
SO_4^{2-}	1.473	109.5	2.399	2.730(14)−3.080(7) ($Cu_{6+12+10}$), 2.67(1)−3.014(5) (Cu_{8+13+8})	2.93(1), 2.82(1)
HPO_3^{2-}	1.516	112.4	2.519	2.66(2)−2.93(2) (Cu_{8+13+8})	2.77(2)
SeO_3^{2-}	1.691	102.4	2.635	2.684(18)−2.948(9) ($Cu_{6+12+10}$)	2.82(1)

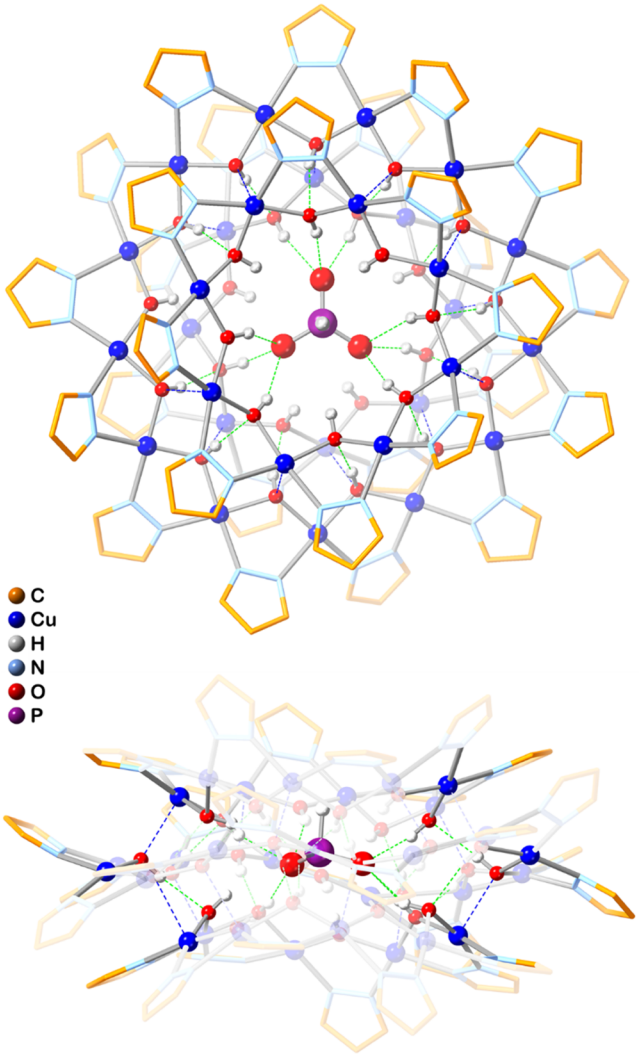

Figure 9. Ball and stick representations of the crystal structure of **2** (top and side views). Green and blue dotted lines indicate O−H···O hydrogen bonds and axial Cu···O interactions, respectively. Counterions, lattice solvent molecules, and C−H bond H atoms are omitted for clarity, and only one component is shown for disordered phosphite and pyrazolate moieties.

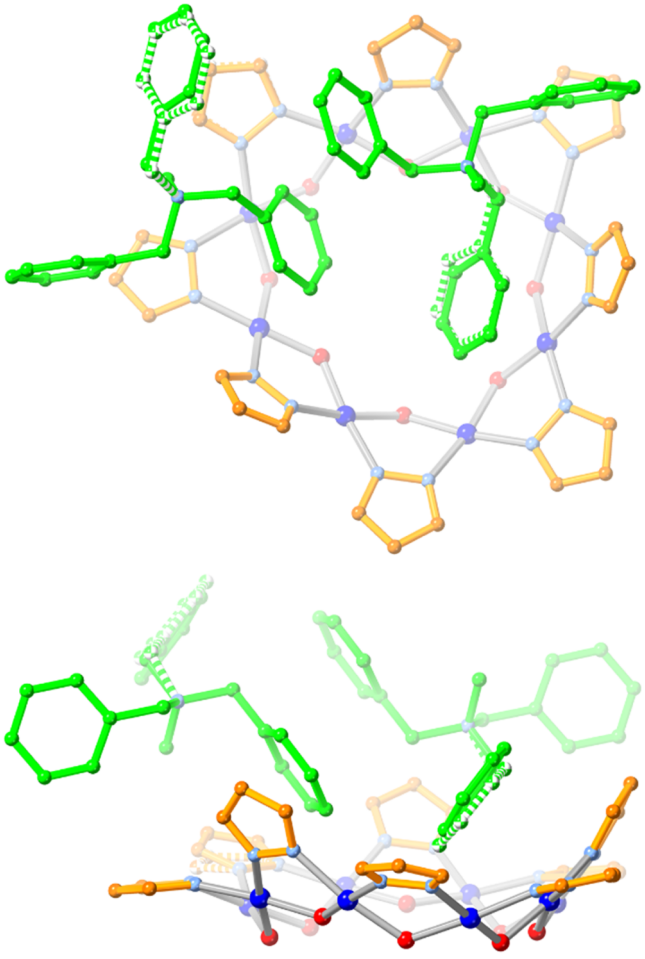

Figure 10. Illustration of the positions of the $TBMA^+$ counterions in the crystal structure of **2**. Dashed bonds indicate a minor disordered benzyl moiety.

3.67(2) and 3.29(2)/3.77(1) Å, respectively (angle between planes: 16.7(8) and 17.2(7)°) (Figure 6). The $TBMA^+$ moieties also engage in edge-to-face aromatic and C−H···π interactions with pyrazole units of the nanojar. In **2**, only one π−π stacking interaction is formed between a pair of phenyl groups from adjacent $TBMA^+$ moieties, with a centroid···centroid distance of 4.279(6) Å and a plane···plane separation of 3.380(9) Å (the angle between phenyl planes is 0°, crystallographically imposed). In addition to edge-to-face aromatic and C−H···π interactions, the $TBMA^+$ moiety in **2** also forms a π−π stacking interaction with the nanojar. The centroid···centroid distance between the disordered phenyl group of $TBMA^+$ and the pyrazolate unit is 3.85(1)/3.94(1) Å, and the plane···plane separation is 3.43(1)/3.15(2)/3.42(2)/3.57(1) Å (angle between planes: 12.4(6)/6.3(6)°). In contrast to **1** and **2**, there are no π−π stacking interactions between adjacent $TBMA^+$ moieties. In addition to edge-to-face aromatic and C−H···π interactions, the $TBMA^+$ moiety in **3** does form π−π stacking interactions with the nanojar, with centroid···centroid distances between the phenyl group of $TBMA^+$ and pyrazolate unit of 3.984(13) and 4.300(11) Å and plane···plane separations of 3.675(15)/3.59(2) and 3.40(3)/3.865(15) Å, respectively (angles between planes: 5.3(8) and 21.1(6)°).

The new nanojar structures made possible by the use of the $TBMA^+$ counterion offer important insights into the anion binding pattern of nanojars. Thus, details of anion binding within the new selenite-incarcerating $Cu_{6+12+10}$ nanojar has been

https://doi.org/10.1021/acs.cgd.1c01361
Cryst. Growth Des. 2022, 22, 1398−1411

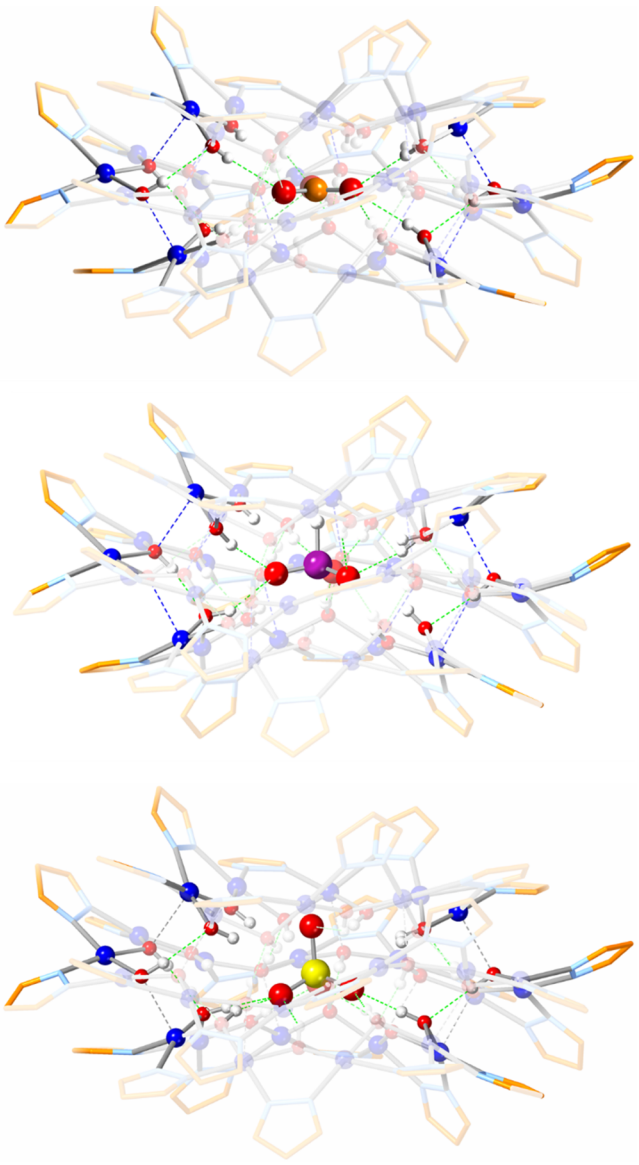

Figure 11. Structural comparison of the nanojars in $(TBMA)_2[HPO_3\subset\{Cu(OH)(pz)\}_{6+12+10}]$ (**2**), $(Bu_4N)_2[CO_3\subset\{Cu(OH)(pz)\}_{8+13+8}]$,[48] and $(Bu_4N)_2[SO_4\subset\{Cu(OH)(pz)\}_{8+13+8}]$.[45] Only one component is shown for disordered selenite, sulfate, and pyrazolate moieties. Green and blue dotted lines indicate O−H···O hydrogen bonds and axial Cu···O interactions, respectively.

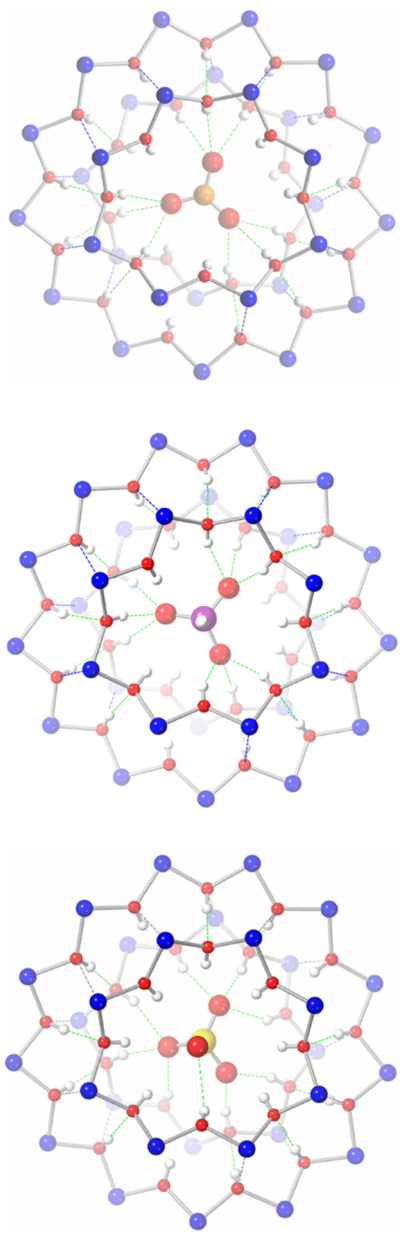

Figure 12. Structural comparison of the anion-binding pockets of the Cu_{29} phosphite (**2**), carbonate, and sulfate nanojars showing their $Cu_{8+13+8}HPO_3$, $Cu_{8+13+8}CO_3$, and $Cu_{8+13+8}SO_4$ cores, respectively (only one component is shown for disordered selenite, sulfate, and pyrazolate moieties). Green and blue dotted lines indicate O−H···O hydrogen bonds and axial Cu···O interactions, respectively.

contrasted with those within the corresponding sulfate-incarcerating $Cu_{6+12+10}$ nanojar. While the host frameworks of these two nanojars are nearly superimposable, the binding of the anion inside the nanojar cavity is markedly different. The most striking dissimilarity is in the orientation of the anion: the SO_4^{2-} ion is pointed inward so that an S−O bond is oriented toward the Cu_6 ring of the nanojar, whereas the SeO_3^{2-} ion is flipped by 180° with the Se atom pointing outward through the center of the Cu_{10} ring and away from the Cu_6 ring. This is likely due to the stereochemically active lone pair of electrons on the Se atom in SeO_3^{2-}. Although this electron pair reduces the average O−E−O angle from 109.5° in sulfate (E = S) to 102.4° in selenite (E = Se), the larger size of Se in comparison to S increases the average E−O bond lengths from 1.473 Å in sulfate to 1.691 Å in selenite. Consequently, the width of the SeO_3^{2-} ion is greater than that of the SO_4^{2-} ion. Because the size of the $Cu_{6+12+10}$ nanojar cavity is essentially the same in the two structures, the larger anion is accommodated by shortening the average H-bond distances between the donor (hydroxide) and acceptor (anion) O atoms from 2.93(1) Å (sulfate) to 2.82(1) Å (selenite).

A similar analysis has been performed on the Cu_{8+13+8} nanojars with three different incarcerated anions: carbonate, sulfate, and phosphite. In this case, the nanojar host framework displays greater flexibility and, although they are quite similar, the three structures are not superimposable. While the average E−O bond lengths in sulfate (1.473 Å) and phosphite (1.516 Å) are similar, the H atom of HPO_3^{2-} allows for an increase in the O−E−O angle from 109.5° in sulfate to 112.4° in phosphite. Therefore, the HPO_3^{2-} ion is wider than the SO_4^{2-} ion, and the

https://doi.org/10.1021/acs.cgd.1c01361
Cryst. Growth Des. 2022, 22, 1398−1411

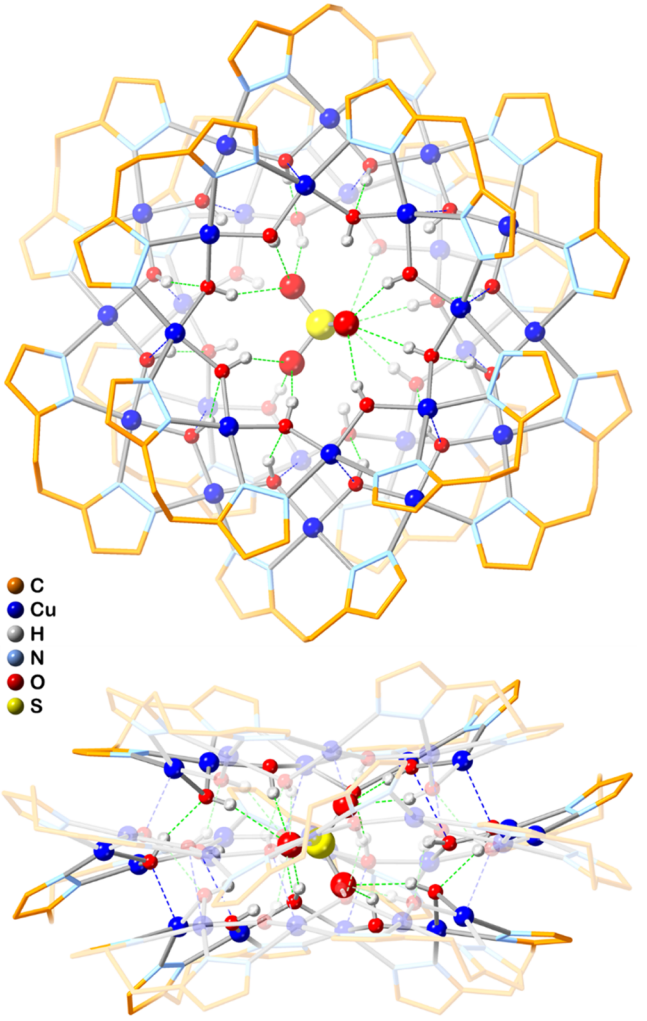

Figure 13. Ball and stick representations of the crystal structure of **3** (top and side views). Green and blue dotted lines indicate O−H···O hydrogen bonds and axial Cu···O interactions, respectively. Lattice solvent molecules and C−H bond H atoms are omitted for clarity.

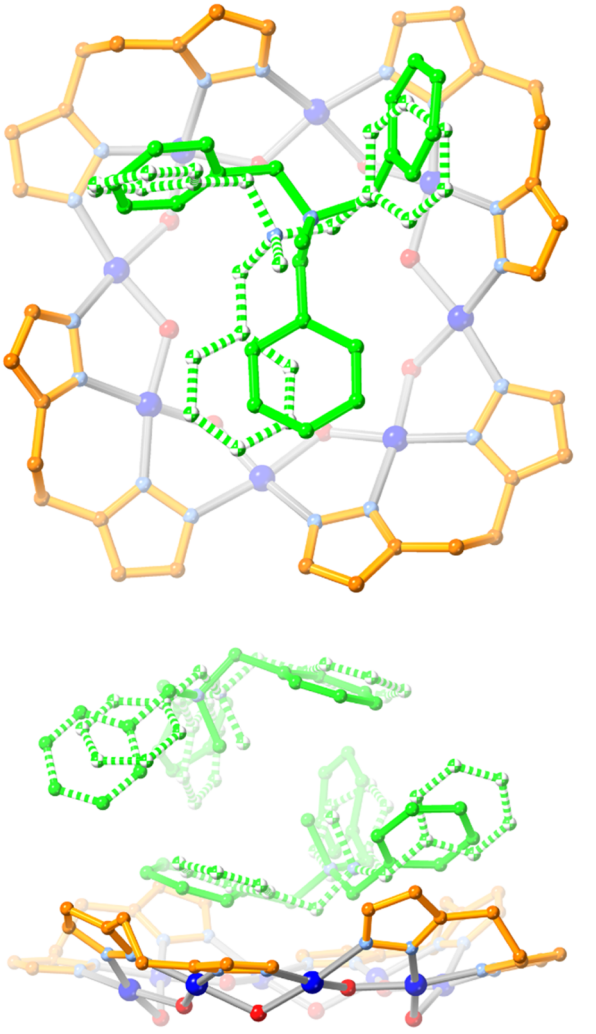

Figure 14. Illustration of the positions of the $TBMA^+$ counterions in the crystal structure of **3**.

CO_3^{2-} ion is significantly smaller (average C−O bond length: 1.284 Å). Again, a shortening of H-bond distances is observed, from 2.86(1) Å (CO_3^{2-}) to 2.82(1) Å (SO_4^{2-}) and 2.77(2) Å (HPO_3^{2-}).

CONCLUSIONS

In this work, we introduce tribenzyl(methyl)ammonium as a new cation for the crystallization of large supramolecular assemblies, exemplified by anion-binding nanojars. The first crystal structures containing $TBMA^+$ presented here are also the first examples of selenite and phosphite ions that are noncovalently bound by a supramolecular assembly and of a nanojar with tethered ligands. An in-depth analysis of these crystal structures provides details not only about the nanojar host structures and hydrogen bonding around the anion guests but also about the intimate phenyl−pyrazolate and phenyl−phenyl aromatic interactions between the $TBMA^+$ counterions and nanojars and between $TBMA^+$ moieties in the crystal lattice.

Structural comparisons of different ions within the same nanojar (SeO_3^{2-} and SO_4^{2-} in the $Cu_{6+12+10}$ nanojar and HPO_3^{2-}, CO_3^{2-}, and SO_4^{2-} in the Cu_{8+13+8} nanojar) reveal different hydrogen-bonding patterns between the incarcerated anion and the OH hydrogen bond donors lining the nanojar cavity. A correlation between the increase in anion size and shortening of the average H-bonding distance between the OH groups of the nanojar and the incarcerated anion is observed. Although a nontethered Cu_{8+12+8} nanojar structure is not yet available for structural and bonding comparisons, the tethered-ligand nanojar **3** is an important example providing details of anion binding in a nanojar with a rigidified outer shell displaying δ/λ chelate-ring isomerism.

Nanojars can be used for the extraction of hydrophilic, small inorganic anion pollutants from water.[56] Herein we have demonstrated that in addition to carbonate, sulfate, phosphate, and arsenate described previously, nanojars can also be used for the binding and extraction of selenite and phosphite ions. Furthermore, the $TBMA^+$ counterion is a welcome addition to the library of compounds displaying "aryl embrace" supramolecular interactions[57,58] and is expected to facilitate the crystallization of other large, hitherto not crystallizable anionic assemblies.

EXPERIMENTAL SECTION

General Considerations. All commercially available chemicals were used as received. $(Bu_4N)_2[SO_4\subset\{Cu_n(OH)_n(pzCH_2CH_2pz)_{n/2}\}]$ (n = 26−30) was synthesized according to a published procedure.[47] NMR spectra were collected on a Jeol JNM-ECZ400S instrument.

https://doi.org/10.1021/acs.cgd.1c01361
Cryst. Growth Des. 2022, 22, 1398−1411

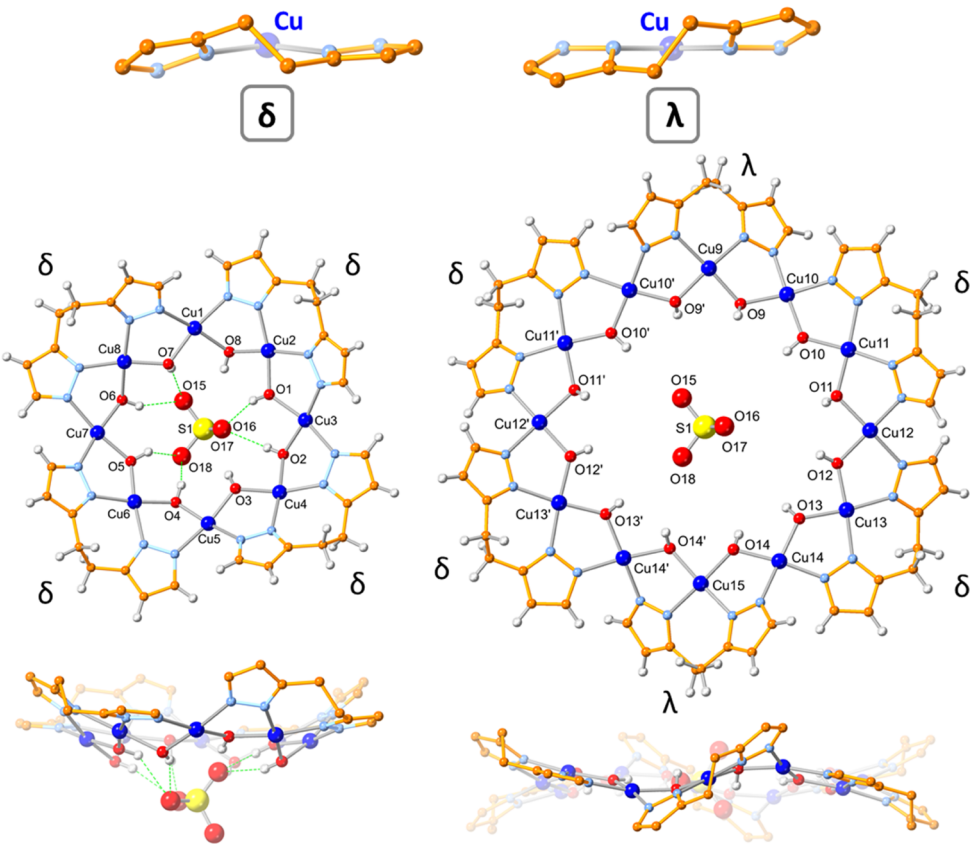

Figure 15. Illustration of the δ/λ chelate-ring conformations (top and side views) in the crystal structure of **3**.

Mass spectrometric analysis of the nanojars was performed with a Waters Synapt G1 HDMS instrument, using electrospray ionization (ESI). Solutions with concentrations of 10^{-4}−10^{-5} M were prepared in CH_3CN. Samples were infused using a syringe pump at 5 μL/min, and nitrogen was supplied as the nebulizing gas at 500 L/h. The electrospray capillary voltage was set to −2.5 or +2.5 kV, respectively, with a desolvation temperature of 110 °C. The sampling and extraction cones were maintained at 40 and 4.0 V, respectively, at 80 °C.

Synthesis of *N,N,N*-Tribenzyl-*N*-methylammonium Iodide (TBMAI). Tribenzylamine (1.0000 g, 3.48 mmol) and iodomethane (5 mL, 11.4000 g, 80.31 mmol) were stirred in a 10 mL round-bottom flask wrapped in aluminum foil at room temperature for 3 days. The excess iodomethane was removed under reduced pressure, and the white residue was washed with diethyl ether (10 mL × 4). The product was obtained as a white powder after drying under high vacuum. Yield: 0.5752 g (39%). ^{1}H NMR (400 MHz, DMSO-d_6): δ 7.59 (d, 6H, 3,5*H*-$C_6H_5CH_2$, J = 6.8 Hz), 7.53−7.45 (m, 9H, 2,4,6*H*- $C_6H_5CH_2$), 4.48 (s, 6H, $C_6H_5CH_2$), and 2.88 (s, 3H, NCH_3) ppm. ^{13}C NMR (101 MHz, DMSO-d_6): δ 133.98, 130.81, 129.47, 128.19, 65.95, and 44.85 ppm.

Synthesis of *N,N,N*-Tribenzyl-*N*-methylammonium Nitrate ($TBMANO_3$). Solutions of TBMAI (0.5752 g, 1.34 mmol) in methanol (10 mL) and silver nitrate (0.2276 g, 1.34 mmol) in methanol (25 mL) were mixed and stirred for 15 min. The silver iodide precipitate was filtered off and washed with methanol (5 mL). The filtrate was evaporated under reduced pressure, leaving behind a white crystalline solid in quantitative yield (0.488 g). ^{1}H NMR (400 MHz, DMSO-d_6): δ 7.59 (d, 6H, 3,5*H*-$C_6H_5CH_2$, J = 6.4 Hz), 7.53−7.44 (m, 9H, 2,4,6*H*-$C_6H_5CH_2$), 4.47 (s, 6H, $C_6H_5CH_2$), and 2.89 (s, 3H, NCH_3) ppm. ^{13}C NMR (101 MHz, DMSO-d_6): δ 133.97, 130.81, 129.48, 128.18, 66.18, and 44.83 ppm.

Synthesis of $(Bu_4N)_2[SeO_3\subset\{Cu(OH)(pz)\}_n]$ (n = 27−29, 31−33). $Cu(NO_3)_2{\cdot}2.5H_2O$ (1.0000 g, 4.30 mmol) and pyrazole (0.2927 g, 4.30 mmol) were dissolved in 20 mL THF in a 50 mL round-bottom flask. Na_2SeO_3 (0.7435 g, 4.30 mmol) was added and the mixture stirred. Then, NaOH (0.3326 g, 8.31 mmol) and tetrabutylammonium hydroxide (55% in H_2O, 0.1380 g, 0.29 mmol) were added and the reaction mixture was stirred in a stoppered flask at room temperature for 3 days. The precipitate was then filtered off and washed with THF. The deep blue filtrate was evaporated under reduced pressure, leaving behind a deep blue residue. The residue was dissolved in 10 mL of THF and was filtered. Evaporation of the THF under high vacuum afforded a dark blue powder. Yield: 0.6537 g. ESI-MS (−): m/z 2056, n = 27; m/z 2130, n = 28; m/z 2204, n = 29; m/z 2352, n = 31; m/z 2425, n = 32; m/z 2499, n = 33.

Synthesis of $(Bu_4N)_2[HPO_3\subset\{Cu(OH)(pz)\}_n]$ (n = 27−32). $Cu(NO_3)_2{\cdot}2.5H_2O$ (1.0000 g, 4.30 mmol) and pyrazole (0.2927 g, 4.30 mmol) were dissolved in 20 mL of THF in a 50 mL round-bottom flask. $Na_2HPO_3{\cdot}5H_2O$ (0.9287 g, 4.30 mmol) was added and the mixture stirred. Then, NaOH (0.3326 g, 8.31 mmol) and tetrabutylammonium hydroxide (55% in H_2O, 0.1380 g, 0.29 mmol) were added and the reaction mixture was stirred in a stoppered flask at room temperature for 3 days. The precipitate was then filtered off and washed with THF. The deep blue filtrate was evaporated under reduced pressure, leaving behind a deep blue residue. The residue was dissolved in 10 mL of THF and filtered. Evaporation of the THF under high vacuum afforded a dark blue powder. Yield: 0.6143 g. ESI-MS (−): m/z 2033, n = 27; m/z 2107, n = 28; m/z 2181, n = 29; m/z 2254, n = 30; m/z 2328, n = 31; m/z 2402, n = 32.

X-ray Crystallography. Colorless single crystals of $TBMANO_3$ suitable for X-ray diffraction analysis were grown by vapor diffusion of diethyl ether into an ethanol solution. Dark blue nanojar single crystals were obtained by dissolving 1 equiv (based on the average oligomer size) of the nanojar mixture in the form of the Bu_4N^+ salt and 2 equiv of $TBMANO_3$ in 1,2-dichlorobenzene/benzonitrile (1:1) (**1**) or nitrobenzene (**2**, **3**) without the use of heat or sonication, followed by filtration and vapor diffusion of hexanes (**1**) or pentane (**2**, **3**) into the solutions at room temperature. Once removed from the mother liquor, the crystals are very sensitive to solvent loss under ambient conditions and were mounted quickly under a cryostream (150 K) to prevent decomposition. X-ray diffraction data were collected from a single

https://doi.org/10.1021/acs.cgd.1c01361
Cryst. Growth Des. 2022, 22, 1398−1411

Table 2. Crystallographic Data for $(TBMA)NO_3$ and 1−3

	$TBMANO_3$	1·solvent	2·solvent	3·solvent
formula	$C_{23}H_{27.52}N_2O_{3.76}$	$C_{129.96}H_{177.31}Cl_{2.65}Cu_{28}N_{58}O_{31}Se$	$C_{143}H_{175}Cu_{29}N_{62}O_{36}P$	$C_{184.21}H_{234.79}Cu_{28}N_{60.23}O_{36.45}S$
FW (g mol^{-1})	392.16	5000.22	5212.07	5687.13
cryst syst	monoclinic	monoclinic	monoclinic	orthorhombic
space group	$C2/c$ (No. 15)	$P2_1/n$ (No. 14)	$C2/c$ (No. 15)	$Pnn2$ (No. 34)
a (Å)	16.6234(6)	20.6039(7)	31.955(7)	16.3369(5)
b (Å)	10.7069(4)	28.761(1)	27.199(10)	25.1450(9)
c (Å)	23.7244(9)	35.8544(11)	26.279(9)	26.4742(9)
α (deg)	90.000	90.000	90.000	90.000
β (deg)	101.8841(16)	90.988(1)	115.526(18)	90.000
γ (deg)	90.000	90.000	90.000	90.000
V (Å^3)	4132.1(3)	21243.8(12)	20610(12)	10875.4(6)
Z	8	4	4	2
D_{calc} (g·cm^{-3})	1.261	1.563	1.680	1.737
μ (mm^{-1})	0.692	3.982	3.004	2.762
θ range (deg)	3.81−80.08	2.64−79.86	2.21−28.36	2.04−28.28
no. of rflns collected	14571	170842	159577	87664
R_{int}	0.0262	0.0671	0.1276	0.0594
no. of obsd rflns ($I > 2\sigma(I)$)	3714	35942	14601	18514
no. of data/restraints/params	4294/582/433	44269/1905/2825	25637/1491/1608	23648/1320/1777
GOF (on F^2)	1.048	1.020	1.013	1.030
R factors ($I > 2\sigma(I)$)	R1 = 0.0473, wR2 = 0.1239	R1 = 0.0779, wR2 = 0.2148	R1 = 0.0536, wR2 = 0.1359	R1 = 0.0449, wR2 = 0.1144
R factors (all data)	R1 = 0.0538, wR2 = 0.1304	R1 = 0.0870, wR2 = 0.2201	R1 = 0.1121, wR2 = 0.1774	R1 = 0.0665, wR2 = 0.1279
max peak/hole (e Å^{-3})	0.203/−0.243	1.427/−1.500	1.271/−0.653	1.066/−0.680
CCDC no.	2118047	2117297	2117298	2117299

crystal mounted atop a MiTeGen micromesh mount under Fomblin oil either on a Bruker AXS D8 Quest diffractometer equipped with a Photon III-C14 charge-integrating and photon-counting pixel array detector (CPAD), a microsource X-ray tube, and a laterally graded multilayer (Goebel) mirror for monochromatization using Cu Kα (λ = 1.54178 Å) radiation ($TBMANO_3$, **1**) or on a Bruker AXS D8 Quest diffractometer equipped with a Photon II charge-integrating pixel array detector (CPAD) using graphite monochromated Mo Kα (λ = 0.71073 Å) radiation (**2**, **3**). The data were collected using APEX3,[59] integrated using SAINT,[60] and scaled and corrected for absorption and other effects using SADABS.[61] The structures were solved by employing direct methods using ShelXS or ShelXT[62] and refined by full-matrix least-squares on F^2 using ShelXL.[63] C−H hydrogen atoms were placed in idealized positions and refined using the riding model. Crystallographic data are summarized in Table 2, and additional refinement details are given below.

In $TBMANO_3$, one of the phenyl rings was refined as disordered. The two disordered moieties were restrained to have similar geometries. U^{ij} components of ADPs for disordered atoms closer to each other than 2.0 Å were restrained to be similar. Subject to these conditions, the occupancy ratio was refined to 0.401(10)/0.599(10). An ethanol molecule was disordered across an inversion center, with the hydroxyl unit H-bonded to one of two nitrate anions related by the inversion center. The methylene C atom overlapped with the inversion-related counterpart of the methyl C atom and vice versa. The ethyl group was further disordered over two positions, for which again the methylene C atom and the inversion-related methyl C atom overlapped. The O−C and C−C distances were restrained to target values (1.43(2) and 1.53(2) Å, respectively). U^{ij} components of ADPs for ethanol atoms closer to each other than 2.0 Å were restrained to be similar. Subject to these conditions, the ethyl occupancy rates were refined to 0.387(4)/0.113(4). The nitrate anion showed substantial disorder, induced by both the ethanol disorder and the presence or absence of a water molecule between nitrate anions related by a 2-fold rotation axis. The anion was refined as disordered over three positions and orientations: moiety A (compatible with the ethanol hydroxyl moiety pointing toward the nitrate and H-bonded to it), moiety B (associated with the water molecule and incompatible with the hydroxyl unit), and the minor moiety C compatible with either the methyl or hydroxyl ethanol ends. The three disordered moieties were restrained to have similar geometries. The less prevalent moieties B and C were also restrained to be close to planar. U^{ij} components of ADPs for disordered atoms closer to each other than 2.0 Å were restrained to be similar. Subject to these conditions, the occupancy rates were refined to 0.387(4)/0.113(4). The two disordered moieties were restrained to have similar geometries. U^{ij} components of ADPs for disordered atoms closer to each other than 2.0 Å were restrained to be similar. Subject to these conditions the occupancy rates were refined to 0.642(3), 0.261(2), and 0.096(2), respectively. The water H atom positions were refined, and O−H and H···H distances were restrained to 0.84(2) and 1.36(2) Å, respectively. One H atom position was restrained to be hydrogen-bonded to a nitrate O atom (H5OA to O1B). The ethanol H atom was restrained to be H-bonded to O3A.

In **1**, the SeO_3^{2-} anion was refined as disordered by rotation. The two disordered moieties were restrained to have similar geometries. U^{ij} components of ADPs for disordered atoms closer to each other than 2.0 Å were restrained to be similar. Subject to these conditions, the occupancy ratio was refined to 0.672(6)/0.328(6). Hydroxyl H atom positions were refined, and O−H distances were restrained to 0.84(2) Å. Several hydroxyl H atom positons were further restrained on the basis of hydrogen-bonding considerations. Three pyrazole ligands were refined as being disordered. For each the two disordered moieties were restrained to have similar geometries. Four of the six moieties were restrained to be coplanar with the copper ions they were bonded to. U^{ij} components of ADPs for disordered atoms closer to each other than 2.0 Å were restrained to be similar. Subject to these conditions, the occupancy ratio was refined to 0.677(12)/0.323(12) (pyrazole of N3), 0.621(11)/0.379(11) (pyrazole of N41), and 0.642(15)/0.358(15) (pyrazole of N47). The $TBMA^+$ cation was disordered (1:1) across an inversion center over two half-occupied positions. Each position was incompatible with its symmetry-equivalent counterpart across the inversion center. The two cation moieties were restrained to have similar geometries. All bonds of the CH_2 groups toward the central carbon atom were restrained to be similar to each other. U^{ij} components of ADPs for disordered atoms closer to each other than 2.0 Å were restrained to be similar. Two 1,2-dichlorobenzene molecules were refined as disordered. All 1,2-dichlorobenzene molecules were restrained to have similar geometries, and all benzene rings were

https://doi.org/10.1021/acs.cgd.1c01361
Cryst. Growth Des. 2022, 22, 1398−1411

constrained to resemble ideal hexagons with C−C bond distances of 1.39 Å. No attempts were made to ensure full occupancy for all solvate sites. A minor ill-defined residual electron density around some pentane and 1,2-dichlorobenzene molecules was ignored. Subject to these conditions, the occupancy rates were refined to the values given in the _atom_site_ in the CIF file. The structure contained an additional 3892 Å^3 of solvent-accessible voids. The content of the voids resembled highly disordered benzonitrile and hexane molecules but were too disordered for a meaningful and stable refinement. The structure factors were instead augmented via reverse Fourier transform methods using the SQUEEZE routine as implemented in the program Platon.[64] The resultant FAB file containing the structure factor contribution from the electron content of the void space was used together with the original *hkl* file in the further refinement (the FAB file with details of the SQUEEZE results is appended to the CIF file). The SQUEEZE procedure corrected for 1009 electrons within the solvent-accessible voids.

In **2**, the oxygen atoms of the HPO_3^{2-} anion were 6-fold disordered, by a 2-fold disorder around a rotation axis and an additional 3-fold general disorder. The P and H atoms were disordered by only the 2-fold rotation. All O···O distances were restrained to be similar to each other. Subject to these conditions, the occupancy rates were refined to two times 0.2303(16), two times 0.1487(16), and two times 0.1209(16). The position of the H atom was freely refined. Four pyrazole ligands were refined as disordered: one around a 2-fold axis in a 1:1 ratio (involving N29) and the other three by general disorder. All disordered pyrazole moieties were restrained to have geometries similar to that of another nondisordered pyrazole (of N1 and N2). U^{ij} components of ADPs for disordered atoms closer to each other than 2.0 Å were restrained to be similar. Subject to these conditions, the occupancy ratios were refined to 0.62(2)/0.38(2) (pz of N5, N6), to 0.63(2)/0.37(2) (pz of N23, N24) and to 0.62(3)/0.38(3) (pz of N27, N28). One benzyl group of the $TBMA^+$ cation was disordered (1:1) due to proximity to the half-occupied P−H unit. The disordered benzyl moieties were restrained to have geometries similar to that of another nondisordered benzyl group. U^{ij} components of ADPs for disordered atoms closer to each other than 2.0 Å were restrained to be similar. Hydroxyl H atom positions were refined, and O−H distances were restrained to 0.84(2) Å. The H atom attached to O15 was 1:1 disordered by a 2-fold axis. Its position was further restrained on the basis of hydrogen-bonding considerations. A solvate nitrobenzene molecule was refined as disordered. The two disordered moieties were restrained to have similar geometries. The nitro N atoms were restrained to be located symmetrically. U^{ij} components of ADPs for disordered atoms closer to each other than 2.0 Å were restrained to be similar. Subject to these conditions, the occupancy ratio was refined to 0.496(9)/0.504(9). The structure contained four additional independent solvent-accessible voids of 3163 Å^3 combined, or ca. 16% of the unit cell volume. The residual electron density peaks were not arranged in an interpretable pattern. The structure factors were instead augmented via reverse Fourier transform methods using the SQUEEZE routine as implemented in the program Platon.[64] The resultant FAB file containing the structure factor contribution from the electron content of the void space was used together with the original *hkl* file in the further refinement (the FAB file with details of the SQUEEZE results is appended to the CIF file). The SQUEEZE procedure corrected for 929 electrons within the solvent-accessible voids.

3 was refined as a two-component inversion twin. The BASF parameter was refined to 0.356(18). Hydroxyl H atom positions were refined, and O−H distances were restrained to 0.84(2) Å. Positions of H atoms H1O and H5O were further restrained on the basis of hydrogen-bonding considerations. The oxygen atoms of the SO_4^{2-} anion were disordered (1:1) around a 2-fold axis located at the position of the sulfur atom. The cation and surrounding solvate molecules were disordered around a 2-fold axis. The disorder ratio for the cation was 1:1. Solvate molecules (nitrobenzene and pentane) were further disordered by general disorder. Additional pentane solvate molecules were present: one located on a 2-fold axis (not disordered) and one in a general position (ill-defined). The two cations were restrained to have similar geometries (SAME command). For the pivot cation, the three benzyl groups were also restrained to have similar geometries. A nitrobenzene molecule was located directly on the 2-fold axis but with the nitro group at an angle to this axis and was refined as 1:1 disordered. It was found to be partially occupied, and the phenyl ring was disordered with two partially occupied pentane molecules (which were symmetry-equivalent and mutually exclusive). The other end of each pentane molecule was in turn disordered with another nitrobenzene molecule. Its occupancy was refined independently. All nitrobenzene moieties were restrained to have similar geometries. For the first nitrobenzene molecule, the two N−O bonds and the N−C−C angles were each restrained to be similar in length, and the nitro group was restrained to be planar. For both nitrobenzene molecules, phenyl rings were restrained to be coplanar with the N atom. C−C bonds and C−C−C angles of pentane molecules were restrained to target values. For the ill-defined pentane, the distance between C99 and C102 was restrained to be at least 3.00(2) Å. U^{ij} components of ADPs for disordered atoms closer to each other than 2.0 Å were restrained to be similar. For the ill-defined pentane, atoms were also restrained to be close to isotropic. Subject to these conditions, the occupancy of the first nitrobenzene (of N30) was refined to two times 0.382(9), that of the pentane to two times 0.118(9), and that of the second nitrobenzene (of N31) to 0.737(12).

■ ASSOCIATED CONTENT

Supporting Information

The Supporting Information is available free of charge at https://pubs.acs.org/doi/10.1021/acs.cgd.1c01361.

Isotopic distributions of ESI-MS peaks and additional crystallographic information (thermal ellipsoid plots, packing diagrams, and bonding data) (PDF)

Accession Codes

CCDC 2117297−2117299 and 2118047 contain the supplementary crystallographic data for this paper. These data can be obtained free of charge via www.ccdc.cam.ac.uk/data_request/cif, or by emailing data_request@ccdc.cam.ac.uk, or by contacting The Cambridge Crystallographic Data Centre, 12 Union Road, Cambridge CB2 1EZ, UK; fax: +44 1223 336033.

■ AUTHOR INFORMATION

Corresponding Author

Gellert Mezei − *Department of Chemistry, Western Michigan University, Kalamazoo, Michigan 49008, United States;* orcid.org/0000-0002-3120-3084; Email: gellert.mezei@wmich.edu

Authors

Wisam A. Al Isawi − *Department of Chemistry, Western Michigan University, Kalamazoo, Michigan 49008, United States*

Matthias Zeller − *Department of Chemistry, Purdue University, West Lafayette, Indiana 47907, United States;* orcid.org/0000-0002-3305-852X

Complete contact information is available at: https://pubs.acs.org/10.1021/acs.cgd.1c01361

Notes

The authors declare no competing financial interest.

■ ACKNOWLEDGMENTS

This material is based on work supported by the National Science Foundation under Grant No. CHE-1808554.

REFERENCES

(1) Pincus, L. N.; Rudel, H. E.; Petrović, P. V.; Gupta, S.; Westerhoff, P.; Muhich, C. L.; Zimmerman, J. B. Exploring the Mechanisms of Selectivity for Environmentally Significant Oxo-Anion Removal during Water Treatment: A Review of Common Competing Oxo-Anions and Tools for Quantifying Selective Adsorption. *Environ. Sci. Technol.* **2020**, *54*, 9769−9790.

(2) Tan, L. C.; Nancharaiah, Y. V.; van Hullebusch, E. D.; Lens, P. N. L. Selenium: Environmental Significance, Pollution, and Biological Treatment Technologies. *Biotechnol. Adv.* **2016**, *34*, 886−907.

(3) Lemly, A. D. Aquatic Selenium Pollution is a Global Environmental Safety Issue. *Ecotoxicol. Environ. Saf.* **2004**, *59*, 44−56.

(4) Poehlein, A.; Daniel, R.; Schink, B.; Simeonova, D. D. Life Based on Phosphite: a Genome-Guided Analysis of Desulfotignum Phosphitoxidans. *BMC Genomics* **2013**, *14*, 753.

(5) Pasek, M. A.; Sampson, J. M.; Atlas, Z. Redox Chemistry in the Phosphorus Biogeochemical Cycle. *Proc. Natl. Acad. Sci. U. S. A.* **2014**, *111*, 15468−15473.

(6) Ewens, S. D.; Gomberg, A. F. S.; Barnum, T. P.; Borton, M. A.; Carlson, H. K.; Wrighton, K. C.; Coates, J. D. The Diversity and Evolution of Microbial Dissimilatory Phosphite Oxidation. *Proc. Natl. Acad. Sci. U. S. A.* **2021**, *118*, No. e2020024118.

(7) McDonald, A. E.; Grant, B. R.; Plaxton, W. C. Phosphite (Phosphorous acid): Its Relevance in the Environment and Agriculture and Influence on Plant Phosphate Starvation Response. *J. Plant Nutr.* **2001**, *24*, 1505−1519.

(8) Havlin, J. L.; Schlegel, A. J. Review of Phosphite as a Plant Nutrient and Fungicide. *Soil Syst.* **2021**, *5*, 52.

(9) Correll, D. L. The Role of Phosphorus in the Eutrophication of Receiving Waters: A Review. *J. Environ. Qual.* **1998**, *27*, 261−266.

(10) Szklarek, S.; Górecka, A.; Wojtal-Frankiewicz, A. The Effects of Road Salt on Freshwater Ecosystems and Solutions for Mitigating Chloride Pollution − A Review. *Sci. Total Environ.* **2022**, *805*, 150289.

(11) Chakrabarti, P. Anion Binding Sites in Protein Structures. *J. Mol. Biol.* **1993**, *234*, 463−482.

(12) Molina, P.; Zapata, F.; Caballero, A. Anion Recognition Strategies Based on Combined Noncovalent Interactions. *Chem. Rev.* **2017**, *117*, 9907−9972.

(13) *Supramolecular Chemistry of Anions*; Bianchi, A., Bowman-James, K., García-Espana, E., Eds.; Wiley-VCH: 1997.

(14) Sessler, J. L.; Gale, P. A.; Cho, W.-S. *Anion Receptor Chemistry*; The Royal Society of Chemistry: 2006; Monographs in Supramolecular Chemistry.

(15) *Anion Recognition in Supramolecular Chemistry*; Springer: 2010; Topics in Heterocyclic Chemistry Vol. *24*.

(16) *Anion Coordination Chemistry*; Bowman-James, K., Bianchi, A., García-Espana, E., Eds.; Wiley-VCH: 2012.

(17) Wu, X.; Macreadie, L. K.; Gale, P. A. Anion Binding in Metal-Organic Frameworks. *Coord. Chem. Rev.* **2021**, *432*, 213708.

(18) Manna, U.; Das, G. An Overview of Anion Coordination by Hydroxyl, Amine and Amide Based Rigid and Symmetric Neutral Dipodal Receptors. *Coord. Chem. Rev.* **2021**, *427*, 213547.

(19) Manna, U.; Das, G. An Overview of CO_3^{2-}/HCO_3^- Binding by Aerial CO_2 Fixation within the Self-Assemblies of Hydrogen-Bond Donor Scaffolds. *CrystEngComm* **2021**, *23*, 512−527.

(20) Hu, Y.; Long, S.; Fu, H.; She, Y.; Xu, Z.; Yoon, J. Revisiting Imidazolium Receptors for the Recognition of Anions: Highlighted Research during 2010−2019. *Chem. Soc. Rev.* **2021**, *50*, 589−618.

(21) Tay, H. M.; Beer, P. Optical Sensing of Anions by Macrocyclic and Interlocked Hosts. *Org. Biomol. Chem.* **2021**, *19*, 4652−4677.

(22) Custelcean, R. Iminoguanidines: From Anion Recognition and Separation to Carbon Capture. *Chem. Commun.* **2020**, *56*, 10272−10280.

(23) Zhao, W.; Flood, A. H.; White, N. G. Recognition and Applications of Anion−Anion Dimers Based on Anti-Electrostatic Hydrogen Bonds (AEHBs). *Chem. Soc. Rev.* **2020**, *49*, 7893−7906.

(24) Pal, S.; Ghosh, T. K.; Ghosh, R.; Mondal, S.; Ghosh, P. Recent Advances in Recognition, Sensing and Extraction of Phosphates: 2015 Onwards. *Coord. Chem. Rev.* **2020**, *405*, 213128.

(25) Chen, L.; Berry, S. N.; Wu, X.; Howe, E. N. W.; Gale, P. A. Advances in Anion Receptor Chemistry. *Chem.* **2020**, *6*, 61−141.

(26) Wu, X.; Gilchrist, A. M.; Gale, P. A. Prospects and Challenges in Anion Recognition and Transport. *Chem.* **2020**, *6*, 1296−1309.

(27) Taylor, M. S. Anion Recognition Based on Halogen, Chalcogen, Pnictogen and Tetrel Bonding. *Coord. Chem. Rev.* **2020**, *413*, 213270.

(28) Pancholi, J.; Beer, P. D. Halogen Bonding Motifs for Anion Recognition. *Coord. Chem. Rev.* **2020**, *416*, 213281.

(29) Kashyap, S.; Singh, R.; Singh, U. P. Inorganic and Organic Anion Sensing by Azole Family Members. *Coord. Chem. Rev.* **2020**, *417*, 213369.

(30) Lai, Z.; Zhao, T.; Sessler, J. L.; He, Q. Bis−Calix[4]pyrroles: Preparation, Structure, Complexation Properties and Beyond. *Coord. Chem. Rev.* **2020**, *425*, 213528.

(31) Wang, D.-X.; Wang, M.-X. Exploring Anion−π Interactions and Their Applications in Supramolecular Chemistry. *Acc. Chem. Res.* **2020**, *53*, 1364−1380.

(32) John, E. A.; Massena, C. J.; Berryman, O. B. Helical Anion Foldamers in Solution. *Chem. Rev.* **2020**, *120*, 2759−2782.

(33) Scheiner, S.; Michalczyk, M.; Zierkiewicz, W. Coordination of Anions by Noncovalently Bonded σ-Hole Ligands. *Coord. Chem. Rev.* **2020**, *405*, 213136.

(34) Wang, H.; Ji, X.; Ahmed, M.; Huang, F.; Sessler, J. L. Hydrogels for Anion Removal from Water. *J. Mater. Chem. A* **2019**, *7*, 1394−1403.

(35) He, Q.; Vargas-Zúñga, G. I.; Kim, S. H.; Kim, S. K.; Sessler, J. L. Macrocycles as Ion Pair Receptors. *Chem. Rev.* **2019**, *119*, 9753−9835.

(36) Boer, S. A.; Foyle, E. M.; Thomas, C. M.; White, N. G. Anion Coordination Chemistry Using O−H Groups. *Chem. Soc. Rev.* **2019**, *48*, 2596−2614.

(37) Eytel, L. M.; Fargher, H. A.; Haley, M. M.; Johnson, D. W. The Road to Aryl CH···Anion Binding Was Paved with Good Intentions: Fundamental Studies, Host Design, and Historical Perspectives in CH Hydrogen Bonding. *Chem. Commun.* **2019**, *55*, 5195−5206.

(38) Davis, J. T.; Gale, P. A.; Quesada, R. Advances in Anion Transport and Supramolecular Medicinal Chemistry. *Chem. Soc. Rev.* **2020**, *49*, 6056−6086.

(39) Akhtar, N.; Biswas, O.; Manna, D. Biological Applications of Synthetic Anion Transporters. *Chem. Commun.* **2020**, *56*, 14137−14153.

(40) Mezei, G.; Baran, P.; Raptis, R. G. Anion Encapsulation by Neutral Supramolecular Assemblies of Cyclic Cu^{II} Complexes: A Series of Five Polymerization Isomers, $[\{cis\text{-}Cu^{II}(\mu\text{-OH})(\mu\text{-pz})\}_n]$, n = 6, 8, 9, 12, and 14. *Angew. Chem., Int. Ed.* **2004**, *43*, 574−577.

(41) Fernando, I. R.; Surmann, S. A.; Urech, A. A.; Poulsen, A. M.; Mezei, G. Selective Total Encapsulation of the Sulfate Anion by Neutral Nano-Jars. *Chem. Commun.* **2012**, *48*, 6860−6862.

(42) Ahmed, B. M.; Mezei, G. From Ordinary to Extraordinary: Insights into the Formation Mechanism and pH-Dependent Assembly/Disassembly of Nanojars. *Inorg. Chem.* **2016**, *55*, 7717−7728.

(43) Ahmed, B. M.; Calco, B.; Mezei, G. Tuning the Structure and Solubility of Nanojars by Peripheral Ligand Substitution, Leading to Unprecedented Liquid−Liquid Extraction of the Carbonate Ion from Water into Aliphatic Solvents. *Dalton Trans.* **2016**, *45*, 8327−8339.

(44) Al Isawi, W. A.; Zeller, M.; Mezei, G. Capped Nanojars: Synthesis, Solution and Solid-State Characterization, and Atmospheric CO_2 Sequestration by Selective Binding of Carbonate. *Inorg. Chem.* **2021**, *60*, 13479−13492.

(45) Ahmed, B. M.; Hartman, C. K.; Mezei, G. Sulfate-Incarcerating Nanojars: Solution and Solid-State Studies, Sulfate Extraction from Water, and Anion Exchange with Carbonate. *Inorg. Chem.* **2016**, *55*, 10666−10679.

(46) Ahmed, B. M.; Mezei, G. Accessing the Inaccessible: Discrete Multinuclear Coordination Complexes and Selective Anion Binding Attainable Only by Tethering Ligands Together. *Chem. Commun.* **2017**, *53*, 1029−1032.

(47) Al Isawi, W. A.; Salome, A. Z.; Ahmed, B. M.; Zeller, M.; Mezei, G. Selective Binding of Anions by Rigidified Nanojars: Sulfate vs. Carbonate. *Org. Biomol. Chem.* **2021**, *19*, 7641−7654.

https://doi.org/10.1021/acs.cgd.1c01361
Cryst. Growth Des. 2022, 22, 1398−1411

(48) Ahmed, B. M.; Szymczyna, B. R.; Jianrattanasawat, S.; Surmann, S. A.; Mezei, G. Survival of the Fittest Nanojar: Stepwise Breakdown of Polydisperse Cu_{27}−Cu_{31} Nanojar Mixtures into Monodisperse $Cu_{27}(CO_3)$ and $Cu_{31}(SO_4)$ Nanojars. *Chem. Eur. J.* **2016**, *22*, 5499−5503.
(49) Mezei, G. Incarceration of One or Two Phosphate or Arsenate Species within Nanojars, Capped Nanojars and Nanohelicages: Helical Chirality from Two Closely-Spaced, Head-to-Head PO_4^{3-} or AsO_4^{3-} Ions. *Chem. Commun.* **2015**, *51*, 10341−10344.
(50) Marquardt, A. Ueber Einige Derivate des Tribenzylamins. *Ber. Deutsch. Chem. Ges.* **1886**, *19*, 1027−1031.
(51) Gagné, O. C.; Hawthorne, F. C. Bond-Length Distributions for Ions Bonded to Oxygen: Results for the Non-Metals and Discussion of Lone-Pair Stereoactivity and the Polymerization of PO_4. *Acta Crystallogr., Sect. B: Struct. Sci., Cryst. Eng. Mater.* **2018**, *B74*, 79−96.
(52) Based on crystal structures of the noncoordinated ion (such as in ammonium salts) in the Cambridge Structural Database.
(53) Lindblow-Kull, C.; Kull, F. J.; Shrift, A. Single Transporter for Sulfate, Selenate, and Selenite in *Escherichia Coli* K-12. *J. Bacteriol.* **1985**, *163*, 1267−1269.
(54) Bisson, C.; Adams, N. B. P.; Stevenson, B.; Brindley, A. A.; Polyviou, D.; Bibby, T. S.; Baker, P. J.; Hunter, C. N.; Hitchcock, A. The Molecular Basis of Phosphite and Hypophosphite Recognition by ABC-Transporters. *Nat. Commun.* **2017**, *8*, 1746.
(55) Adams, N. B. P.; Robertson, A. J.; Hunter, C. N.; Hitchcock, A.; Bisson, C. Phosphite Binding by the HtxB Periplasmic Binding Protein Depends on the Protonation State of the Ligand. *Sci. Rep.* **2019**, *9*, 10231.
(56) Mezei, G. Selective Extraction of Anions from Solutions. US Patent 9,901,901 B2 (Feb 27, 2018), US Patent 10,087,197 B2 (Oct 2, 2018), European Patent 2852558 B1 (Sept 9, 2020).
(57) Dance, I. π−π Interactions: Theory and Scope. In *Encyclopedia of Supramolecular Chemistry*; Atwood, J. L., Steed, J. W., Eds.; Taylor & Francis Group: 2004.
(58) James, S. L. π−π Stacking as a Crystal Engineering Tool. In *Encyclopedia of Supramolecular Chemistry*; Atwood, J. L., Steed, J. W., Eds.; Taylor & Francis Group: 2004.
(59) *APEX3*; Bruker AXS: 2016.
(60) *SAINT v.8.38A*; Bruker: 2017.
(61) Krause, L.; Herbst-Irmer, R.; Sheldrick, G. M.; Stalke, D. Comparison of Silver and Molybdenum Microfocus X-Ray Sources for Single-Crystal Structure Determination. *J. Appl. Crystallogr.* **2015**, *48*, 3−10.
(62) Sheldrick, G. M. A Short History of *SHELX*. *Acta Crystallogr., Sect. A: Found. Crystallogr.* **2008**, *A64*, 112−122.
(63) Sheldrick, G. M. Crystal Structure Refinement with SHELXL. *Acta Crystallogr., Sect. C: Struct. Chem.* **2015**, *71*, 3−8.
(64) van der Sluis, P.; Spek, A. L. BYPASS: An Effective Method for the Refinement of Crystal Structures Containing Disordered Solvent Regions. *Acta Crystallogr., Sect. A: Found. Crystallogr.* **1990**, *A46*, 194−201.

https://doi.org/10.1021/acs.cgd.1c01361
Cryst. Growth Des. 2022, 22, 1398−1411